

where z is the vertical depth (in meters), defined to be zero at the surface and increasing downward. We used Monte Carlo simulations to estimate the systematic uncertainties in the global fit from the contamination of multiple-photon events, background events, and limited sample sizes. We find that the various effects tend to cancel each other. A conservative estimate of the total uncertainty in λ_a is

$$\lambda_a = 59 \pm 1(\text{stat}) \pm 3(\text{syst}) \text{ m} \quad (9)$$

Figure 3A shows the observed linear dependence of $1/\lambda_{\text{bub}}$ on depth. This depth dependence is steeper than would be expected if the bubble number density were constant and only the bubble sizes decreased under the hydrostatic pressure ($1/\lambda_{\text{bub}} \propto z^{-2/3}$). The shaded area in Fig. 3B corresponds to the uncertainty in the bubble shapes—that is, in the average scattering angle. Also shown in Fig. 3B are results from the measurements on the Vostok and Byrd ice cores. Figure 4 shows the measured absorption lengths at different depths.

We measured the propagation parameters of visible light in the South Pole ice to an accuracy of $\sim 5\%$, using the calibration setup of the AMANDA detector (these measurements were made without extracting ice samples). The small uncertainty in the measured value of λ_a was achievable only because of the long travel times of photons in the bubbly ice. Alternative explanations to the observed photon time distributions (such as that the time distributions are caused by fluorescence in the medium) are extremely unlikely. Our results are also incompatible with a localized bubble concentration as the cause of the observed time smearing. The examined ice volume, 0.8 to 1 km below the surface, has an extremely long absorption length, comparable with the quality of the ultrapure water used in the IMB and Kamiokande proton-decay and neutrino experiments (14, 15) and more than twice as long as the best value reported for laboratory ice (13).

The results of this study suggest that the ice cap is indeed an ideal medium for a neutrino telescope. If the absorption length does not deteriorate with depth, the volume of a future muon and neutrino detector to be deployed at greater depth can be made significantly larger than previously anticipated because the PMTs can be spaced farther apart. A linear extrapolation of our data would indicate that bubbles vanish at ~ 1150 m at the South Pole. The data from Vostok and Byrd (Fig. 3B) show, however, that the rate of bubble disappearance becomes somewhat slower toward the end of the transition process (16).

REFERENCES AND NOTES

1. P. K. F. Grieder, talk given at "Trends in Astroparticle Physics," Stockholm, September 1994 [*Nucl. Phys. B* (suppl.), in press].
2. NESTOR Collaboration, in *Proceedings of the Workshop on High Energy Neutrino Astrophysics*, V. J. Stenger *et al.*, Eds. (World Scientific, Singapore, 1992).
3. H. Shoji and Ch. C. Langway Jr., *Nature* **298**, 548 (1982).
4. A. J. Gow and T. Williamson, *J. Geophys. Res.* **80**, 5101 (1975).
5. H. Shoji and Ch. C. Langway Jr., *J. Phys. (Paris) (Suppl. 3)* **48**, C1-551 (1987).
6. N. I. Barkov and V. Ya. Lipenkov, *Mater. Glyatsiolog. Issled.* **51**, 178 (1985).
7. T. Hondoh *et al.*, *J. Incl. Phen.* **8**, 17 (1990); T. Uchida, personal communication.
8. AMANDA Collaboration (P. Askebjerg *et al.*), in preparation.
9. T. Miller *et al.*, in *Proceedings of 23rd International Cosmic Ray Conference*, D. A. Leahy *et al.*, Eds. (World Scientific, Singapore, 1993), vol. 4, p. 557.
10. S. Chandrasekhar, *Rev. Mod. Phys.* **15**, 1 (1943).
11. A. Ishimaru, *J. Opt. Soc. Am.* **68**, 8 (1978); M. S. Patterson *et al.*, *Appl. Opt.* **28**, 12 (1989).
12. H. C. van de Hulst, *Light Scattering by Small Particles* (Wiley, New York, 1957).
13. T. C. Grenfell and D. K. Perovich, *J. Geophys. Res.* **86**, 7447 (1981); S. G. Warren, *Appl. Opt.* **23**, 1206 (1984).
14. R. Becker-Szendy *et al.*, *Nuclear Instrum. Methods*, in press.
15. K. Inoue, thesis, Institute of Cosmic Ray Research, University of Tokyo (1993).
16. During the Antarctic summer of 1994–1995, we plan to collect new calibration data with the same system to establish the wavelength dependence of the optical properties of the South Pole ice (P. Askebjerg *et al.*, in preparation).
17. We thank B. Koci and the entire Polar Ice Coring Office organization for support with the ice drilling. This work was supported by the National Science Foundation (USA), the K. A. Wallenberg Foundation (Sweden), the Swedish Natural Science Research Council, the G. Gustafsson Foundation (Sweden), Swedish Polar Research, the Graduate School of the University of Wisconsin, Madison (USA), and the University of California at Irvine (USA).

24 August 1994; accepted 13 December 1994

Viscous Dissipation in Three-Dimensional Convection with Temperature-Dependent Viscosity

S. Balachandar,* D. A. Yuen, D. M. Reuteler, G. S. Lauer

Numerical simulations of three-dimensional convection with temperature-dependent viscosity and viscous heating at realistic Rayleigh numbers for Earth's mantle reveal that, in the strongly time-dependent regime, very intense localized heating takes place along the top portion of descending cold sheets and also at locations where the ascending plume heads impinge at the surface. For a viscosity contrast of 100, these localized heat sources exceed the internal heating due to the radioactive decay of chondritic materials by more than an order of magnitude. The horizontally averaged viscous dissipation is concentrated in the top of the convecting layer and has a magnitude comparable with that of radioactive heating.

Viscous dissipation is an irreversible process accompanying fluid motion and has generally been studied in the high Mach number regimes. However, even at the low speeds of fluid motion in Earth's mantle, the contribution from viscous heating can be significant because of the great distances involved (1). This potentially important role played by viscous heating and its coupling to temperature-dependent viscosity on mantle dynamics has long been recognized (2–5). Recent two-dimensional (2D) time-dependent studies (6) have shown that viscous heating can trigger heating instabilities in the transition zone as a result of the interaction of a hot plume with the endothermic phase transition (7). In this report, we investigate the phenomenon of viscous heating coupled

with the temperature-dependent viscosity in three dimensions at high Rayleigh numbers and discuss the nature of the intense shear heating that is produced both in hot rising plumes and along the descending cold sheets. Such localized heating helps explain the source of hot anomalies adjacent to subducting regions (8) and the thinning of the lithosphere above hot upwellings (9). This phenomenon of localized viscous heating does not occur in the ordinary Boussinesq convection, which can be studied in laboratory experiments (10), but instead must be studied numerically.

We used a spectral-transform technique (11) to solve the relevant conservation equations. The numerical model includes the effects of both viscous heating and adiabatic cooling but no internal heating. We considered an aspect ratio of 5 by 5 by 1, with unity being the depth of the layer. The dimensionless equations for the conservation of mass, momentum, and energy in terms of the nondimensional velocity u , temperature T , and dynamical

S. Balachandar, Department of Theoretical and Applied Mechanics, University of Illinois, Urbana, IL 61801, USA. D. A. Yuen, D. M. Reuteler, G. S. Lauer, Minnesota Supercomputer Institute and Department of Geology and Geophysics, University of Minnesota, Minneapolis, MN 55415, USA.

*To whom correspondence should be addressed.

pressure p were cast in the infinite Prandtl number limit (12) in which the control variables are the dimensionless dissipation number D and the surface Rayleigh number Ra_s (13). A linear Newtonian rheology was assumed with viscosity varying only with temperature as

$$\eta(T) = \eta_0 \exp(-\beta T) \quad (1)$$

where η_0 is the surface viscosity and β controls the viscosity contrast between the cold fluid at the surface and the hot fluid at the bottom. With this dependence, the strongest viscosity variations occur at low temperatures. An exponential dependence of viscosity on temperature is a good model for capturing the physics of convection with variable viscosity and has been used in earlier theoretical and experimental investigations (14).

The viscous heating term, Φ , is positive and therefore always acts as a heat input to the system. The nondimensional form of this viscous heating is

$$\Phi = \frac{D}{2Ra_s} \frac{\eta(T)}{\eta_0} \left[\left(\frac{\partial u_i}{\partial x_j} + \frac{\partial u_j}{\partial x_i} \right) \left(\frac{\partial u_i}{\partial x_j} + \frac{\partial u_j}{\partial x_i} \right) \right] \quad (2)$$

This viscous heating term imposes a strong nonlinearity because of the temperature-dependent viscosity and represents a local source of intense heating in regions of high velocity gradients and low temperatures (15). We have considered two models: model 1, with depth-dependent density, thermal expansivity, and thermal conductivity (16), and model 2, with constant thermodynamic and transport properties except viscosity.

For model 1 the simulation was started from an initial condition of constant viscosity, and the viscosity contrast was increased incrementally to 100. The value of Ra_s for the run described below is 10^5 , which results in a bottom Rayleigh number of 1.7×10^6 . Figure 1 shows both 3D and side views of the lateral thermal anomaly at three snapshots in time (17). Over hundreds of millions of years, significant evolution of both the hot plumes and cold sheets was observed. In the simulations, the cold sinking sheets became plume-like structures and extended well into the lower mantle (18). In contrast, the hot rising plumes were relatively narrow even in the lower mantle and did not extend all the way into the upper mantle. Yet disconnected patches of hot material, which are associated with these rising plumes, could be observed near the top surface. These flattened, hot, disconnected plume heads were the result of intense viscous heating generated by the large strain suffered by the hot plumes as they impinged on the top boundary layer

(lithosphere) and spread horizontally underneath. The simultaneous cooling of these hot plumes near the surface also tended to enhance the thermal contrast produced by viscous heating. These disconnected, hot, spreading plume heads seem characteristic of the strongly time-dependent nature of temperature-dependent viscosity convection and are conspicuously absent in the constant viscosity convection at comparable levels of con-

vective vigor corresponding to an effective Rayleigh number of 10^6 (19).

The spatial complexity of the distribution of viscous heating is shown in Fig. 2. Typically most of the heating was in regions of descending cold sheets and also surprisingly in ascending hot plumes (20). The largest viscous heating was observed precisely where the ascending plumes impinge on the upper surface. Although viscosity in this region is not high, because the

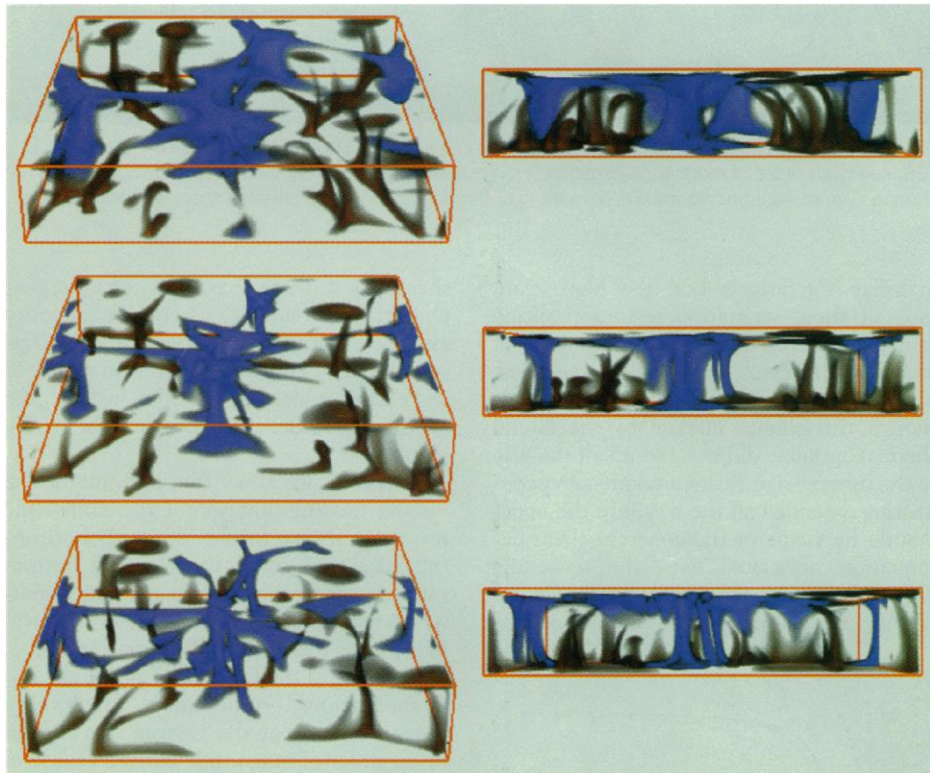


Fig. 1. A 3D volume rendering (17) of the temperature anomaly, $\delta T = T - \langle T \rangle$, where $\langle T \rangle$ is the horizontally averaged temperature; δT at three different times is shown. Time increases from top to bottom. The first frame is obtained after sufficiently long integration that a steady state is obtained, and subsequent frames are $\delta t = 0.0015$ (190 million years) apart. On the left a 3D view is shown. The corresponding side view, shown on the right, shows the vertical structure of these positive and negative thermal anomalies. The brown color indicates hot ascending plumes, and the blue color indicates cold sinking sheets.

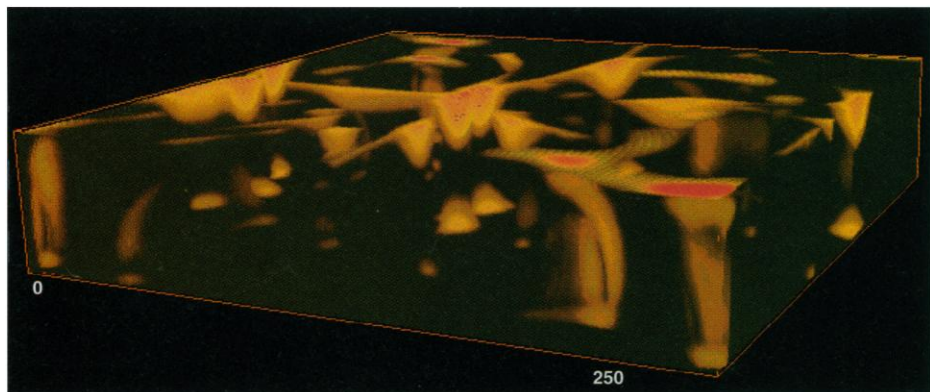


Fig. 2. A 3D volume rendering of the viscous heat generation at a time corresponding to that of the last frame of Fig. 1. The region of most intense heating, marked by the bright red color, is localized to where the upwelling plumes impinge on the surface and spread horizontally.

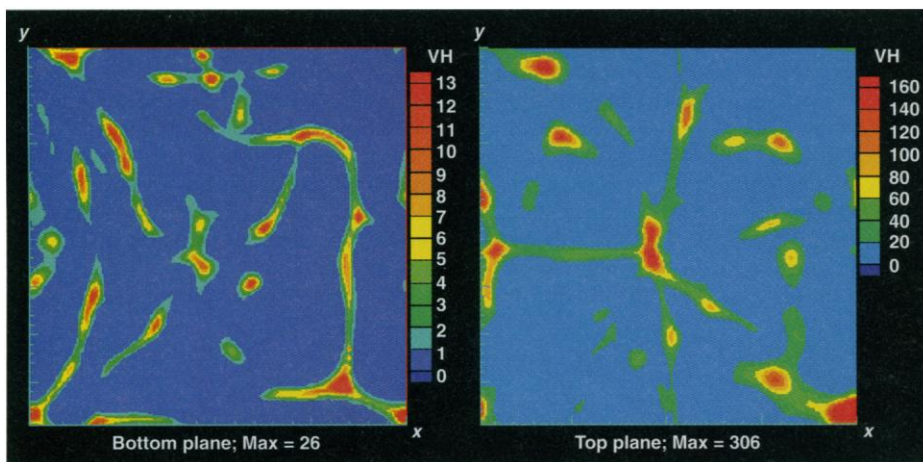


Fig. 3. Viscous heating (VH) at the base and surface of the model. The maximum viscous heating reaches 306, nearly an order of magnitude larger than radiogenic heating, where the hot plume impinges on the surface. The corresponding maximum heating at the descending cold sheet is approximately 185.

material is relatively hot, the high strain rates at these stagnation regions resulting from the depth-dependent properties of model 1 (21) result in strong viscous heating. The results of model 1 imply that, although the plumes marked by the lateral thermal anomaly did not extend all the way to the surface, significant amounts of viscous heating extended all the way into the upper mantle by virtue of the coherent shear deformation associated with the upwelling plume flow. On the other hand, viscous heating produced along the cold descending

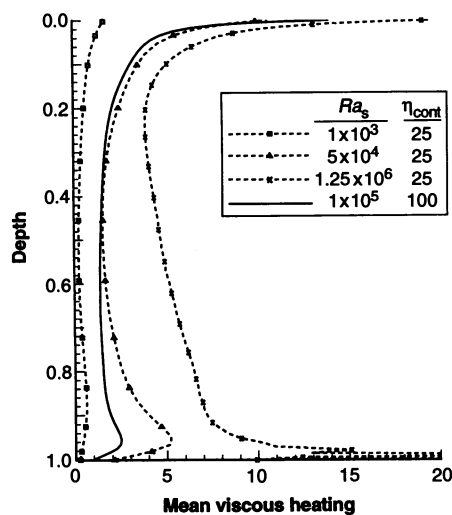


Fig. 4. Horizontally averaged viscous heating as a function of depth for four different cases. The solid curve corresponds to model 1 with a viscosity contrast of 100, $Ra_s = 10^5$, and depth-dependent α and κ . The other three curves are for model 2 with a viscosity contrast of 25 and Ra_s values of 10^3 , 5×10^4 , and 1.25×10^6 , respectively, and constant α and κ . Because of a boundary effect, the $Ra_s = 1.25 \times 10^6$ curve near depth 1.0 has a secondary peak with a mean viscous heating >20 (not shown).

sheets was restricted to only a narrow region near the top surface, where the viscosity associated with the cold sheets is large. The peak values of viscous heating in the cold descending sheets were about 60% of the maximum values produced in the rising plumes.

In Fig. 3 we show the contours of the viscous heating function at the same time instant as shown for Fig. 2, on 2D horizontal cross sections at the top and bottom surfaces, respectively. A maximum nondimensional viscous heating of 306 (22) was found near the lower right corner of Fig. 3, right panel, at the top surface where the hot plume impinges on the surface. The level of viscous heating at the bottom was smaller by an order of magnitude partly because of the decrease by a factor of 100 in the viscosity. In comparison, the magnitude of radioactive heating from chondritic abundance lies between 10 and 15 (23). Thus, even with this rather modest temperature-dependent viscosity model, there were localized regions near the surface where viscous heating can be more than an order of magnitude greater than heating from radioactivity. These regions of intense viscous heating were persistent features of the flow, and they moved about slowly.

Heating along cold descending sheets can lead to lubrication and the natural formation of a weakened zone adjacent to subducting slabs (24). The localized heating at the top of plumes and along cold descending sheets decreases the viscous resistance at both these sites, and this would result in an enhanced strain rate, which could feed further into the heating process. This nonlinear feedback maintains the enhanced localized heating within the convective flow.

Even the horizontally averaged magnitude of viscous heating (shown in Fig. 4 as

the solid curve) was significant and was comparable with radiogenic heating close to the surface. Also shown as the dashed curves are the results for model 2. They show that viscous heating increased markedly with the vigor of convection (25). This result would mean that viscous heating could be stronger in the young Earth. In model 2, viscous heating occurred primarily at the descending cold sheets and, unlike the case for model 1, in model 2, viscous heating associated with the ascending hot plumes was smaller because the plumes were less vigorous owing to the constant thermal expansivity [see also (21)].

Many other factors in the mantle can influence the generation of this localized heating. One is the non-Newtonian nature of mantle rheology, which has a tendency to concentrate upwelling and downwelling flows (26). Internal heating in the upper mantle would further focus the downwelling sheets (27), increasing the amplitude of viscous heating in descending flows. An increase in the vertical rheological stratification would also lead to the formation of thinner jets (28), and this process would also enhance viscous heating of the diapiric flows. Viscous heating could also contribute to the superplume events (29) because of the large convective vigor that might be associated with this type of instability.

REFERENCES AND NOTES

1. In slow viscous flow the strength of viscous dissipation scales as D/Ra , where D is the dimensionless dissipation number and Ra is the Rayleigh number; D is proportional to the depth of the layer. For Earth's mantle the averaged value of D is between 0.3 and 0.5 [G. T. Jarvis and D. P. McKenzie, *J. Fluid Mech.* **96**, 515 (1980); A. M. Leitch, D. A. Yuen, G. Sewell, *Earth Planet. Sci. Lett.* **102**, 213 (1990)].
2. H. R. Shaw, *J. Petrol.* **10**, 510 (1969); U. Nitsan, *J. Geophys. Res.* **78**, 1395 (1973).
3. N. Fujii and S. Uyeda, *ibid.* **79**, 3367 (1974).
4. G. Schubert, C. Froidevaux, D. A. Yuen, *ibid.* **81**, 3525 (1976).
5. D. A. Yuen, F. Quareni, H.-J. Hong, *Nature* **326**, 67 (1987).
6. V. Steinbach and D. A. Yuen, *Earth Planet. Sci. Lett.* **127**, 67 (1994).
7. Viscous heating from the plume impinging at the phase boundary in layered convection decreases the viscosity and allows for the hot lower mantle material to flow easily through the endothermic phase transition, giving rise to an additional source of heat. This temperature increase further decreases the viscosity and allows for the liberation of more latent heat. This process allows for high temperatures to be produced locally in the transition zone [see (6)].
8. D. L. Turcotte and G. Schubert, *J. Geophys. Res.* **78**, 5876 (1973).
9. D. L. Turcotte and S. H. Emerman, *Tectonophysics* **94**, 39 (1983); D. A. Yuen and L. M. Fleitout, *Nature* **313**, 125 (1985).
10. P. L. Olson and H. A. Singer, *J. Fluid Mech.* **158**, 511 (1985); R. W. Griffiths, *ibid.* **166**, 115 (1986).
11. S. Balachandar and D. A. Yuen, *J. Comput. Phys.* **113**, 62 (1994). We used a Fourier-Chebyshev expansion with 75 grid points in the vertical and 160 in each of the two horizontal directions. Periodic boundary conditions were imposed along the sides,

and the top and bottom boundaries were stress-free, impermeable, and held at different constant temperatures. There was no internal heating. The thermal and velocity spectra showed at least three to four orders of magnitude decay with wave number along all three directions, indicating adequate spatial resolution.

12. The equation for conservation of mass takes the form of the anelastic approximation in which the time derivative of the density is neglected. Y. Ogura and N. A. Phillips, *J. Atmos. Sci.* **19**, 173 (1962).
13. The dissipation number D is given by $\alpha gh/C_p$, where α is the thermal expansivity, g is the gravitational acceleration, h is the depth of the mantle, and C_p is the specific heat [see also (1)]. The value of Ra_s is given by $\alpha_0 g \Delta T h^3 / \nu_0 \kappa_0$, where the subscript "0" indicates surface value and κ and ν are, respectively, the thermal diffusivity and the kinematic viscosity.
14. F. H. Busse and H. Frick, *J. Fluid Mech.* **150**, 451 (1985); D. B. White, *ibid.* **191**, 247 (1988); A. C. Fowler, *Stud. Appl. Math.* **72**, 189 (1985); E. Giannandrea and U. R. Christensen, *Phys. Earth Planet. Inter.* **78**, 139 (1993).
15. The temperature-dependent viscosity introduces variable coefficients into the momentum equation, and therefore the momentum equation is solved iteratively with the generalized minimum residual method [Y. Saad and M. H. Schultz, *Soc. Ind. Appl. Math. J. Sci. Stat. Comput.* **7**, 856 (1986)]. Here the depth-dependent part of the momentum equation is treated as a preconditioner to accelerate convergence.
16. The background adiabatic density, ρ_a , varies with nondimensional depth, z , as $[1 + 2(D/\gamma)z]^{1/2}$, where γ is the Grüneisen parameter. Thermal expansivity decreases with density according to $1/\rho_a^6$, as determined experimentally [A. Chopelas and R. Boehler, *Geophys. Res. Lett.* **19**, 1983 (1992)]. Thermal conductivity is modeled as ρ_a^4 , following phonon conduction [D. L. Anderson, *Phys. Earth Planet. Inter.* **45**, 307 (1987)].
17. K. Chin-Purcell, Preprint 92-141 (Army High Performance Computing Research Center, Minneapolis, 1992). BOB (Brick of Bytes) is an interactive computer program for volume rendering of 3D data on Silicon Graphics workstations.
18. There are no phase transitions in this model [S. Honda, D. A. Yuen, S. Balachandar, D. Reuteler, *Science* **259**, 1308 (1993)].
19. Disconnected hot plumes are observed in high- Ra , constant-viscosity convection in the Boussinesq limit for Ra in excess of 10^7 [A. V. Malevsky and D. A. Yuen, *Geophys. Res. Lett.* **20**, 383 (1993)]. The occurrence of this phenomenon marks the transition of convection to the hard-turbulent regime [F. Heslot, B. Castaing, A. Libchaber, *Phys. Rev. A* **36**, 5870 (1987)].
20. It has been conjectured that, because of the low viscosity in hot plumes, viscous heating be regarded as a second-order effect in the dynamics of plumes [D. E. Loper and F. Stacey, *Phys. Earth Planet. Inter.* **33**, 304 (1983)].
21. In studies of convection with depth-dependent thermal expansivity it has been shown that the hot plumes grow in vigor on their way up because of the increase in buoyancy [S. Balachandar, D. A. Yuen, D. M. Reuteler, *Geophys. Res. Lett.* **19**, 2247 (1992); U. Hansen, D. A. Yuen, S. E. Kroening, T. B. Larsen, *Phys. Earth Planet. Inter.* **77**, 205 (1993)].
22. This number comes directly from numerical evaluation of Eq. 2, the viscous dissipation contribution to the energy equation.
23. The amount of internal heating in the mantle due to radioactive decay is $\sim 6 \times 10^{-12}$ W/kg for average concentrations in chondritic meteorites, which can be regarded as primitive mantle material. This internal heating also appears in nondimensional form as an inhomogeneous source term in the temperature equation [A. M. Leitch and D. A. Yuen, *Geophys. Res. Lett.* **16**, 1407 (1989)].
24. In Boussinesq convection models with plates, weakened zones are positioned adjacent to the descending slabs [H. Schmeling and W. R. Jacoby, *J. Geophys. (London)* **50**, 89 (1981); M. Gurnis, *Geophys. Res. Lett.* **16**, 179 (1989); A. Lenardic and W. M. Kaula, *J. Geophys. Res.* **99**, 15697 (1994)].

25. For model 2, the effective Rayleigh number based on mean temperature is given by $Ra_{eff} = 5 \times Ra_s$, whereas, for model 1, because of the depth-dependent properties, $Ra_{eff} = 4 \times Ra_s$. Thus, the behavior of model 2 at $Ra_s = 5 \times 10^4$ is the closest to that of model 1.
26. U. R. Christensen and D. A. Yuen, *J. Geophys. Res.* **94**, 814 (1989); A. V. Malevsky and D. A. Yuen, *Geophys. Astrophys. Fluid Dyn.* **65**, 149 (1992).
27. D. P. McKenzie, J. M. Roberts, N. O. Weiss, *J. Fluid Mech.* **62**, 465 (1974); S. A. Weinstein, P. L. Olson, D. A. Yuen, *Geophys. Astrophys. Fluid Dyn.* **47**, 157 (1989).

28. P. E. van Keken, D. A. Yuen, A. P. van den Berg, *Earth Planet. Sci. Lett.* **112**, 179 (1992); *Geophys. Res. Lett.* **20**, 1927 (1993).
29. R. L. Larson, *Geology* **19**, 547 (1991).
30. We thank V. C. Steinbach and Yu. Yu. Podladchikov for inspiring discussions that provided the stimulus for this work. This research was supported by the Geochemistry Program and the Division of Mathematical Sciences of the National Science Foundation (NSF DMS 92-01042) and by the National Aeronautics and Space Administration.

28 September 1994; accepted 12 December 1994

Visual Appearance of Matte Surfaces

Shree K. Nayar* and Michael Oren

All visual sensors, biological and artificial, are finite in resolution by necessity. As a result, the effective reflectance of surfaces in a scene varies with magnification. A reflectance model for matte surfaces is described that incorporates the effect of macroscopic surface undulations on image brightness. The model takes into account complex physical phenomena such as masking, shadowing, and interreflections between points on the surface, and it predicts the appearance of a wide range of natural surfaces. The implications of these results for human vision, machine vision, and computer graphics are demonstrated with both real and rendered images of three-dimensional objects. In particular, objects with extremely rough surfaces produce silhouette images devoid of shading, precluding visual perception of the object's shape.

Painters and sculptors use their knowledge of the interaction between light and materials (1, 2) to convey compelling shape cues to an observer (3). Reflection of light by materials may be viewed as the first fundamental process in visual perception by human or machine. All reflectance mechanisms can be broadly classified into two categories: surface and body. In surface reflection, light rays are reflected at the interface between the surface medium and air. With very smooth surfaces, this results in a specular or mirrorlike appearance, where the viewed surface produces a clear virtual image of its surroundings that is geometrically distorted if the surface is not planar (4). The rougher the surface, the more the virtual image becomes blurred, altering surface appearance from shiny to glossy, and even becoming diffuse for very rough surfaces. Surface reflection is common, for instance, in metals.

In body reflection, incident light rays penetrate the surface and are scattered around because of reflections and refractions caused by inhomogeneities within the surface medium. Some of this light energy may be absorbed by the surface or transmitted through it. The remaining light energy finds its way back to the interface to re-emerge as body reflection. As a result of the random subsurface scattering of light, the

emerging light rays are distributed in a wide range of directions, giving the surface a matte appearance. Body reflection predominates in materials like clay, plaster, concrete, and paper. In many other materials, however, both surface and body reflection mechanisms coexist and together determine the final visual appearance. Mathematical models for both reflection mechanisms, based on physical and geometrical optics, have been studied extensively.

For body reflection, numerous models have been suggested for the scattering process (5-7). Among these, Lambert's law (5), proposed in 1760, remains the most widely used in visual psychophysics (8), computational vision (9), remote sensing (10), and computer graphics (11). It predicts that the brightness, or radiance, L_r , of an ideal matte surface point is $\frac{\rho}{\pi} \cos \theta_i$, where ρ , the albedo or reflectivity, represents the fraction of the total incident light reflected by the surface, and θ_i is the incidence angle between the surface normal and the illumination direction. The popularity of Lambert's model can be attributed to its ability to predict with a fair degree of accuracy the appearance of a large spectrum of real materials. Another reason is undoubtedly its simple mathematical form, which lends itself to the prediction of numerous interesting appearance properties; for theoreticians and practitioners alike, the use of Lambert's law is a temptation difficult to resist. Both reasons have led to its widespread use in understanding and emulating perception of im-

Department of Computer Science, Columbia University, New York, NY 10027, USA.

*To whom correspondence should be addressed.